Carbon Nanospheres

Controlled Synthesis of N-Doped Carbon Nanospheres with Tailored Mesopores through Self-Assembly of Colloidal Silica

Gang Wang, Yuhan Sun, Debao Li, Hai-Wei Liang, Renhao Dong, Xinliang Feng,* and Klaus Müllen*

Abstract: Limited strategies have been established to prepare monodisperse mesoporous carbon nanospheres (MCNs) with tailored pore sizes. In this work, a method is reported to synthesize MCNs by combining polymerization of aniline with co-assembly of colloidal silica nanoparticles. The controlled self-assembly behavior of colloidal silica enables the formation of uniform composite nanospheres and convenient modulation over mesopores. After carbonization and removal of sacrificial templates, the resultant MCNs possess tunable mesopores (7–42 nm) and spherical diameters (90–300 nm), as well as high surface area (785–1117 $m^2 g^{-1}$), large pore volume (1.46–2.01 $cm^3 g^{-1}$) and abundant nitrogen moieties (5.54–8.73 at %). When serving as metal-free electrocatalysts for the oxygen reduction reaction (ORR), MCNs with an optimum pore size of 22 nm, compared to those with 7 and 42 nm, exhibit the best ORR performance in alkaline medium.

Mesoporous carbon nanospheres (MCNs) with particle sizes near or below 200 nm have attracted considerable attention for applications in the fields of drug delivery, adsorption, and catalysis, as well as energy storage and conversion because of their superior physical and chemical properties, such as good electrical conductivity, robust mechanical stability, large surface area, enhanced mass transport, and excellent biocompatibility.[1] Although MCNs have been fabricated by nanocasting with mesoporous silica spheres used as a scaffold, which can simultaneously direct the porous structure and spherical morphology,[1a,2] the pore size and morphology of the prepared MCNs were limited by the parent template. An aerogel-assisted self-assembly strat-

egy was also developed to produce MCNs using silicate clusters, colloidal silica, and amphiphilic triblock copolymers as templates.[3] The resultant MCNs showed a tunable pore size with a broad distribution of particle sizes ranging from 50 nm to >1 μm. More recently, a soft-templating method based on polystyrene–polyethylene oxide (PS–PEO) block copolymers was reported to afford N-doped MCNs (N-MCNs) with mesopores tunable from 5.4 to 16 nm.[4] Nevertheless, MCNs with mesopores over 16 nm, which are believed to promote the mass transport properties for various applications,[5] including the oxygen reduction reaction (ORR), have not been achieved.[6] Compared with microporous materials, mesoporous carbons (doped or metal-integrated), especially those with large mesopores, exhibit increased ORR activity, which can be ascribed to enhanced mass transportation by reducing and smoothing the diffusion pathways.[4,6b,7] Unfortunately, no optimum value of MCN mesopore size for ORR activity has been determined because it is challenging to achieve well-defined and tunable porous structures in the mesoscopic range. Therefore, controlling the pore size of MCNs without sacrificing their monodispersity and spherical morphology is highly appealing.

In this work, we develop a strategy for the fabrication of N-MCNs through self-assembly of colloidal silica in the presence of polyaniline (PANI), allowing for the simultaneous morphological control and pore size modulation. The prepared N-MCNs possess tailorable mesopores (7–42 nm) and particle sizes (90–300 nm) as well as high surface area (785–1117 $m^2 g^{-1}$), pore volume (1.46–2.01 $cm^3 g^{-1}$) and nitrogen content (5.54–8.73 at %), which can serve as metal-free electrocatalysts for ORR. N-MCNs with 22 nm-mesopores, compared with those of 7 and 42 nm, exhibit the best ORR performance in alkaline medium, showing high activity (half-wave potential of 0.78 V vs. 0.85 V for Pt/C), large diffusion-limited current (≈ 5.5 mA cm^{-2}), high selectivity (electron-transfer number > 3.86), superior tolerance to methanol, and excellent long-term cycling stability.

The overall synthetic procedure leading to N-MCNs is illustrated in Scheme 1. A stable dispersion of aniline/colloidal silica is pre-formed before the polymerization reaction. Then, the polymerization of aniline and further co-assembly with silica nanoparticles (NPs) are initiated by the addition of ammonium persulfate, allowing the formation of SiO$_2$@PANI composite nanospheres under mild conditions. The aromatic feature and high N/C ratio of PANI ensure homogeneous incorporation of abundant N atoms into the carbon framework during the carbonization process. After removal of silica by etching with HF or NaOH, well-defined mesopores are developed in the N-doped carbon nano-

[*] G. Wang, Dr. H. Liang, Prof. K. Müllen
Max Planck Institute for Polymer Research
Ackermannweg 10, 55128 Mainz (Germany)
E-mail: muellen@mpip-mainz.mpg.de

G. Wang, Prof. Y. Sun, Prof. D. Li
State Key Laboratory of Coal Conversion
Institute of Coal Chemistry, Chinese Academy of Sciences
030001 Taiyuan (China)

Dr. R. Dong, Prof. X. Feng
Center for Advancing Electronics Dresden (CFAED) &
Department of Chemistry and Food Chemistry
Technische Universität Dresden
01062 Dresden (Germany)
E-mail: xinliang.feng@tu-dresden.de

G. Wang
University of Chinese Academy of Sciences
100049 Beijing (China)
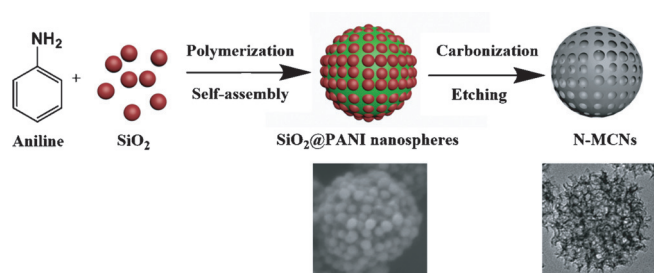
Scheme 1. Illustration of self-assembly of colloidal silica with PANI and the derived N-MCNs.

spheres, affording monodisperse N-MCNs. For clarity, N-MCNs-*x*-*y* refers to samples prepared from silica with *x* nm diameter and carbonized at *y* °C. For comparison, nonporous PANI (Figure 1 c) and its derived nonporous nitrogen-doped carbon (NC) were also prepared using a similar procedure, but in the absence of the colloidal silica template. The fabrication details of all samples in this work are summarized in the Supporting Information.
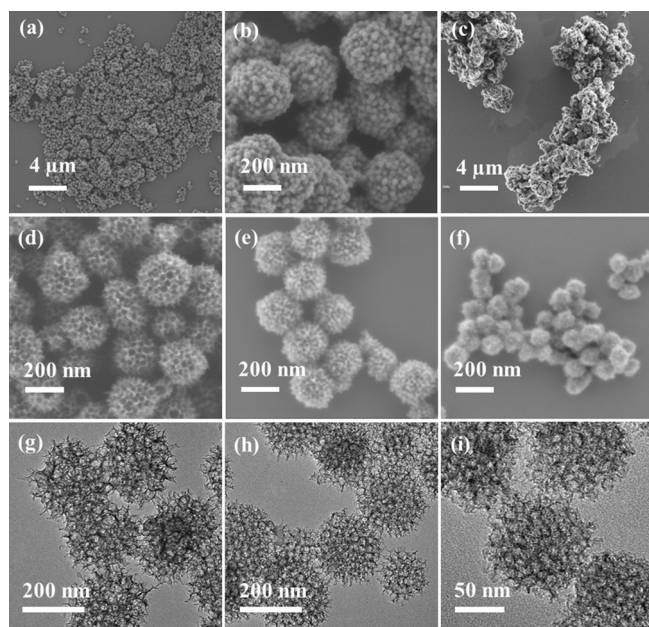

Figure 1. SEM images of SiO$_2$@PANI composite nanospheres (a and b) and nonporous PANI (c). SEM and TEM images of the prepared N-MCNs (d and g: N-MCNs-42; e and h: N-MCNs-22; f and i: N-MCNs-7).

The role of silica in the formation of N-MCNs was first investigated. The presence of colloidal silica significantly influenced the product morphology of PANI. The polymerization of aniline with silica produced monodisperse SiO$_2$@PANI nanospheres, where SiO$_2$ NPs were uniformly embedded into the PANI matrix (Figure 1a,b; Supporting Information, Figure S1a,b). Without silica, aniline polymerized into irregular granules up to tens of micrometers in size with multiple short PANI rods on the bulk surface (Figures 1c and S1c,d). This result suggested that the spherical morphol-

ogy of the SiO$_2$@PANI composite stemmed from the co-assembly of SiO$_2$ NPs and PANI rather than PANI alone. In contrast, polymer nanospheres based on the Stöber synthesis of resorcinol-formaldehyde (RF) resin and polydopamine (PD)[1f,4,8] have a strong capability of forming a spherical morphology. The SiO$_2$ NPs on the surface of the SiO$_2$@PANI spheres could further prevent severe carbon conglutination during high-temperature carbonization, producing discrete SiO$_2$@C nanospheres. After removal of the SiO$_2$ template, MCNs with the desired mesopores were readily obtained. Thus, the colloidal silica used not only functioned as a sacrificial pore-forming agent but also contributed to the spherical morphology and monodispersity of the product. Even though colloidal silica has been frequently used as a hard template to prepare mesoporous carbon,[7b,9] no similar self-assembly behavior or directing functions on product morphology was observed so far.

SEM images (Figure 1 d–f) revealed that the as-formed MCNs completely retained the original spherical morphology of the SiO$_2$@PANI composite without structural collapse, and homogeneous mesopores were clearly observed on the surface of MCNs after carbonization and etching. When colloidal silica with different sizes was used, the particle size as well as the mesopores of MCNs could be effectively adjusted (Figures 1 d–f and S2 d–i). MCNs prepared from silica of 42, 22, and 7 nm had average diameters of 264, 222, and 98 nm, respectively. The porous structure of the MCNs was further confirmed by TEM images (Figure 1 g–i). Structure-defined mesopores were well-developed throughout the entire carbon spheres in all samples, indicating their open porous features. The wall thickness of the mesopores was determined to be 2–4 nm. The XRD patterns of N-MCNs prepared at 800–1000 °C (Figure S3 a) showed two broad peaks at approximately 24° and 44°, corresponding to graphitic carbon (002) and (004), respectively, indicating partial graphitization of MCNs.[10] This result was further evidenced by the Raman spectra (Figure S3 b) and high-resolution TEM image (HRTEM, Figure S4).

Nitrogen adsorption–desorption isotherms were performed to analyze the porosities of the obtained N-MCNs. The results, including Brunauer–Emmett–Teller (BET) surface area, pore volume, and pore size are summarized in Table 1. The isotherms of N-MCNs exhibited type IV isotherm characteristics, indicative of the presence of mesopores (Figure 2 a). The steep and high capillary condensation steps revealed uniform and well-developed mesoporosity with a large mesopore volume.[11] Based on the Barrett–Joyner–

Table 1: Physicochemical properties and average particle size of N-MCNs.

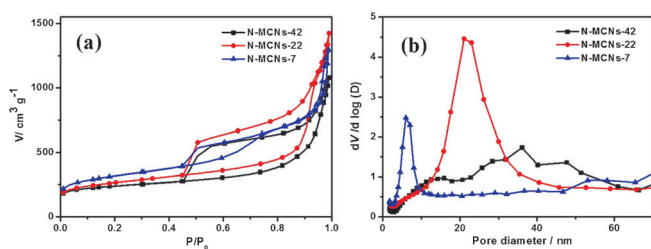| Sample	Surface area [m^2 g^{-1}]	Pore volume [cm^3 g^{-1}]	Pore size [nm]	Particle size [nm]
N-MCNs-42-900	785	1.46	42	264
N-MCNs-22-900	926	2.01	22	222
N-MCNs-7-900	1117	1.77	7	98

Figure 2. N₂ sorption isotherms (a) and pore size distribution (b) of the as-formed N-MCNs.

Halenda model, the pore size distributions were calculated from the adsorption branch of the isotherms and determined to be 42, 22, and 7 nm for N-MCNs-42, -22, and -7 (Figure 2b), respectively, which is highly consistent with the diameter of the silica templates. The BET surface area and pore volume of the corresponding samples ranged from 785 to 1117 $m^2 g^{-1}$ and 1.46 to 2.01 $cm^3 g^{-1}$, respectively, both of which are superior to the values of most MCNs prepared by other methods (Table S1).

Aside from silica templates with different sizes, the feed ratio of template to aniline monomer can be easily modulated to control the wall thickness and surface area of MCNs. As shown in Figure 3a–c, the wall thickness of MCNs was tunable from several tens of nanometers to 2–4 nm at a feed ratio of 1 to 3, without influencing the spherical morphology. The BET surface area of the corresponding samples varied from 590 to 926 $m^2 g^{-1}$. It should be mentioned that this controlled self-assembly method of hard templates to prepare MCNs can be further expanded to polypyrrole, another nitrogen- and carbon-rich polymer precursor. The corresponding carbon nanospheres after carbonization of polypyr-
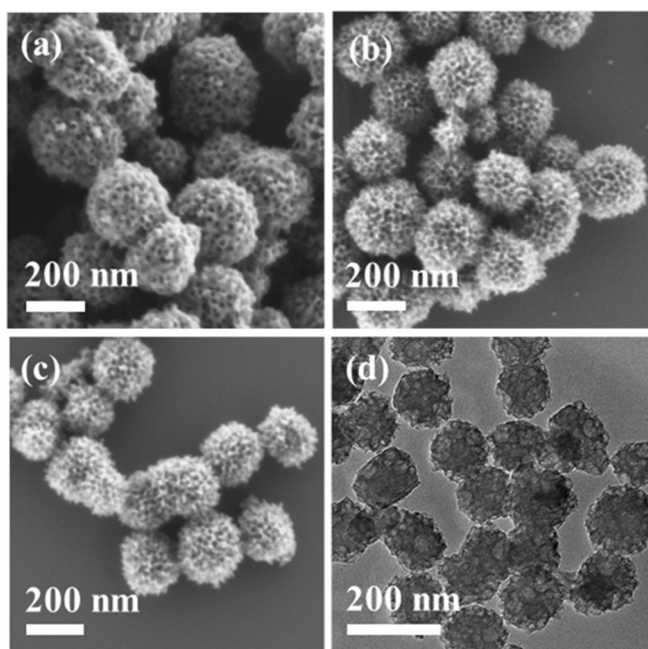
role exhibited similar mesoporosity, spherical morphology, and monodispersity (particle size ≈ 100 nm; Figure 3 d). Another advantage of the as-formed N-MCNs is their excellent solution dispersibility, which is essential for further modification and functionalization toward other applications.[12] After sonicating for a short time, MCNs can be stably dispersed in water for up to one month, likely as a result of the highly uniform particle size and positive charges generated from N-doping (Table S2).

To understand the formation mechanism of SiO₂@PANI nanospheres, a series of samples were collected under different reaction times (t) to directly probe the growth process (Figure S5). By prolonging t from 1 to 24 h, more SiO₂ NPs were assembled into spherical SiO₂@PANI, accompanied by a size increase of SiO₂@PANI from 150 to 250 nm, which may be driven by a combined effect of electrostatic interactions and hydrogen bonding between colloidal silica and PANI. The surface charges of the reaction intermediates were monitored by zeta potential (ζ) measurements (Table S2). Under the experimental conditions, colloidal silica was first dispersed in HCl solution, changing the surface charges of SiO₂ from negative ($\zeta = -44.3$ mV) to positive ($\zeta = 2.37$ mV). Bearing in mind that PANI can be protonated by HCl-doping, positive charges are developed in the polymerization of aniline, as confirmed by the zeta potentials of the prepared SiO₂@PANI ($\zeta = 40.4$ mV) and mesoporous PANI ($\zeta = 43.9$ mV). Therefore, direct assembly of both positively charged SiO₂ and PANI seems unreasonable because of the strong electrostatic repulsion. The halide counteranion (Cl⁻) likely involves and functions between positively charged SiO₂ and PANI through a well-known $S^+X^-I^+$ pathway, which frequently occurs in the synthesis of silica mesophases from acidic medium.[13] Compared with strong electrostatic interactions, H-bonding is relatively weak but is indispensable in the soft-templating synthesis of MCNs.[1b,4] In our system, H-bonding also exists between -OH groups in SiO₂ templates and N−H groups in aniline/PANI, possibly leading to a similar self-assembly behavior. Based on the above analysis, we surmise that the self-assembly of colloidal silica is accomplished in the following manner (Scheme S1): (1) after initiation by the addition of ammonium persulfate, the combination of electrostatic interaction and H-bonding first drives the heterogeneous nucleation and growth of PANI on silica, then directs the adsorption of other free silica NPs; (2) continuous growth of PANI and accumulation of silica produce large SiO₂@PANI assemblies of spherical shapes (Figure S5), which are energetically favorable in solution, and the strong electrostatic repulsion between positively charged SiO₂@PANI assemblies ($\zeta = 40.4$ mV) prevents severe aggregation during the growth process; (3) as a result of the depletion of aniline monomer, the self-assembly of colloidal silica terminates, affording SiO₂@PANI composite nanospheres.

X-ray photoelectron spectroscopy was used to analyze the chemical composition of N-MCNs prepared under different conditions. Three predominant peaks at 285, 400, and 530 eV, corresponding to C 1s, N 1s, and O 1s, respectively, were observed in all samples (Figure S6a), indicating the presence of C, N, and O elements. All of the samples contained
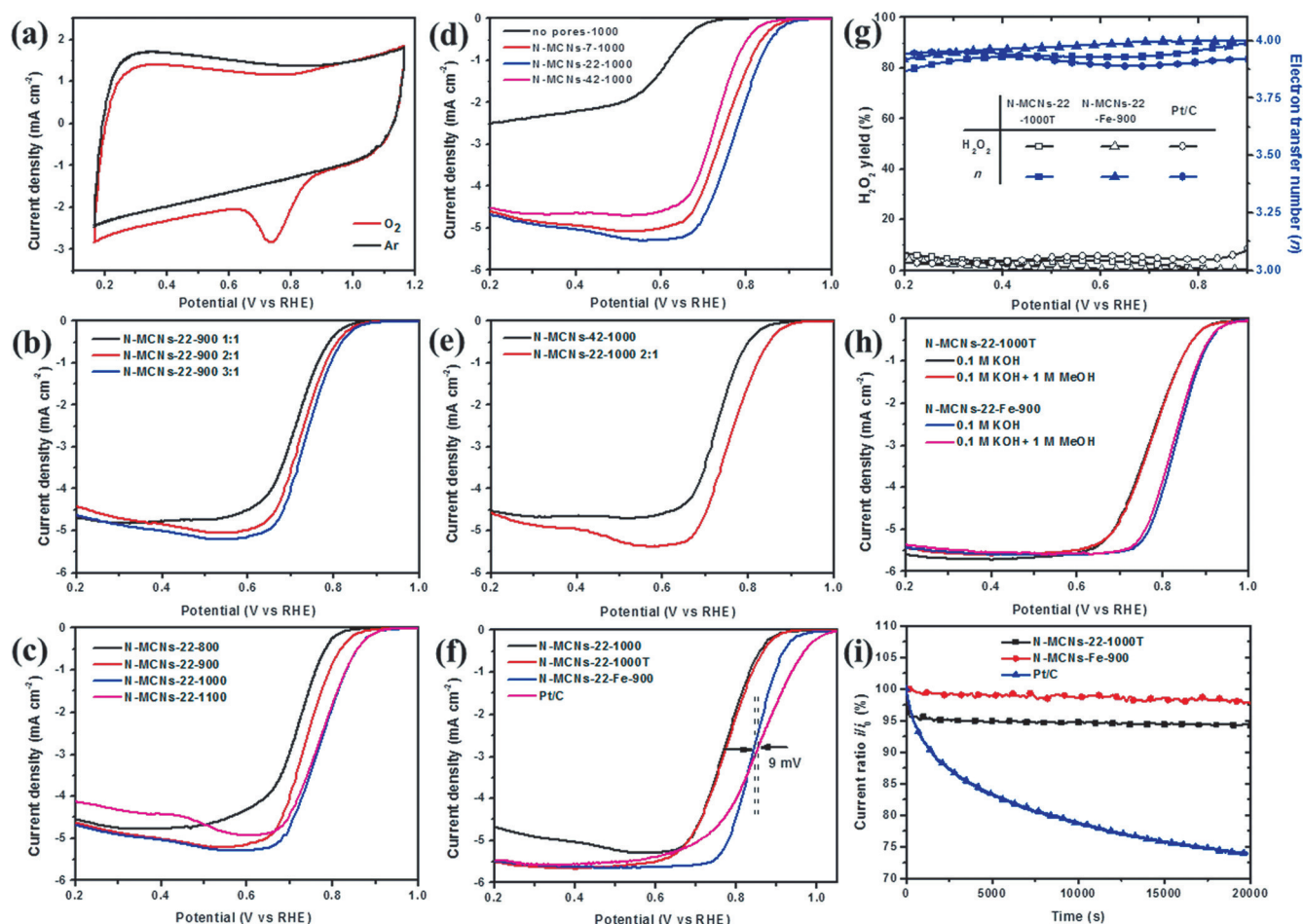

Figure 3. SEM images of MCNs-22 prepared with different feed ratios of SiO₂ to aniline of a) 1:1, b) 2:1 and c) 3:1. d) A typical TEM image of MCNs prepared from polypyrrole.

Figure 4. ORR performance of N-MCNs. a) CV curve of N-MCNs-22-1000. b–f) Linear sweep voltammetry (LSV) curves of catalysts prepared under different feed ratios (b), pyrolysis temperature (c), templates (d–e), and a second thermal treatment and Fe-doping (f) in O_2 saturated 0.1 M KOH with a sweep rate of 10 mVs^{-1} at 1600 rpm. g) H_2O_2 yield and electron transfer number of N-MCNs-22-1000T, N-MCNs-22-Fe-900 and Pt/C. h) LSV curves of N-MCNs-22-1000T and N-MCNs-22-Fe-900 in 0.1 M KOH without and with 1 M MeOH. i) Current-time CA response of N-MCNs-22-1000T, N-MCNs-22-Fe-900 and Pt/C in O_2 saturated 0.1 M KOH at 0.565 V (vs. RHE) at 1600 rpm.

a significant amount of oxygen species (5–6 at %), which are frequently found in carbon materials prepared by hard-templating methods and are mainly derived from the oxygen-doping effect by the inorganic templates.[9c, 14] When elevating the carbonization temperature from 800 to 1000 °C, the carbon content of the N-MCNs samples slightly increased, whereas the nitrogen content decreased from 8.73 to 5.54 at %. The type of nitrogen, which highly determines the performance of electrocatalysts, was further investigated (Figure S6 b–d). The high-resolution N 1s spectrum of N-MCNs-22-800 can be deconvoluted into three different nitrogen species: pyridinic N (398.4 ± 0.1 eV), pyrrolic N (399.8 ± 0.1 eV), and quaternary N (400.9 ± 0.1 eV).[7b, 9a] Quaternary N significantly increased from 54.1 % to 72.8 % (total N content) with increasing carbonization temperature (800–1000 °C), whereas both pyridinic N and pyrrolic N declined, indicating the better thermal stability of quaternary N. The details of this analysis are summarized in Table S3.

ORR is a critical process for many energy storage and conversion devices (fuel cells and metal–air batteries). Many factors associated with electrocatalysts, such as surface area, chemical composition, and porous structure, determine the final electrocatalytic performance by optimization of the active sites and mass transport properties.[7b,9a,b] N-MCNs, possessing tunable N composition, tailored mesopores, and high surface area, can serve as excellent candidates for the ORR. The ORR catalytic activity of the as-prepared N-MCNs was then investigated by cyclic voltammetry (CV) in 0.1 M KOH at room temperature. As shown in Figure 4a, a pronounced peak at approximately 0.75 V versus the reversible hydrogen electrode (RHE) was observed in O_2-saturated electrolyte rather than Ar-saturated electrolyte, indicating pronounced ORR activity. Rotating disk electrode (RDE) measurements were conducted to verify the effects of different reaction parameters, such as feed ratio (template to monomer), pyrolysis temperature, and mesopore size, on the activity of the catalysts. Compared to catalysts prepared at a low feed ratio ($\leq$ 2:1), N-MCNs-22 at a ratio of 3:1 delivered a higher accessible surface area up to 926 m^{2}g^{-1} (vs. 590 m^{2}g^{-1} at 1:1 and 728 m^{2}g^{-1} at 2:1), thus exhibiting a much more

positive onset potential, and half-wave potential ($E_{1/2}$) as well as a larger current density (Figure 4b). With regard to the pyrolysis temperature, the highest $E_{1/2}$ (0.78 V vs. RHE) and largest cathodic current density were achieved by N-MCNs-22-1000 (Figure 4c), which is attributed to its higher content of quaternary N (Table S3). Quaternary N can induce non-uniform electron distribution on adjacent carbon atoms and facilitate O_2 adsorption and dissociation,[15] thus functioning as the efficient active site of ORR.[16]

The pore size effect was further examined by investigating four N-doped samples pyrolyzed at 1000 °C with no pores and with 7, 22, and 42 nm mesopores (Figure 4d). The ORR activities (both the current density and $E_{1/2}$) followed the sequence of N-MCNs-22 > −7 > −42 > non-porous sample. Although N-MCNs-7 had a surface area as high as 1171 $m^2 g^{-1}$ (Table S4), the $E_{1/2}$ (0.75 V) was inferior to that of N-MCNs-22 (0.78 V) with a lower surface area (914 $m^2 g^{-1}$). Considering the favorable contribution of surface area to catalytic activity, the excellent performance of N-MCNs-22 can be attributed to the enhanced mass transport by smoothing the diffusion pathways.[4,7b] Compared with N-MCNs-42, the N-MCNs-22 electrocatalyst with similar surface area (762 $m^2 g^{-1}$) and particle size ($\approx$240 nm) was also prepared at a feed ratio of 2:1. As revealed in Figure 4e, the catalyst with 22 nm mesopores exhibited much higher activity than that with 42 nm mesopores, indicating an optimum mesopore size (22 nm) of N-MCNs for ORR activity. A similar conclusion can also be achieved by analyzing the kinetic current density of the catalysts within the mixed kinetic-diffusion controlled region and normalizing them to the specific surface areas (Tafel plots in Figure S7). Moreover, a large diffusion-limiting current up to 5.5 $mA cm^{-2}$ was achieved for N-MCNs-22-1000T (thermally treated again at 1000 °C), which was slightly higher than that of Pt/C in the range of 0.2–0.65 V. Although the $E_{1/2}$ of N-MCNs-22-1000T (0.78 V) was still lower than that of the state-of-the-art commercial Pt/C catalysts (0.85 V, 20% Pt, BASF), it was comparable to most metal-free N-doped carbon electrocatalysts reported in recent literature (Table S5). To further improve the electrocatalytic performance, we doped iron into MCNs (see the Supporting Information) to construct Fe–Nx center.[9b,17] The as-formed catalyst (N-MCNs-22-Fe-900) possessed similar porous features to N-MCNs, including high surface area, large pore volume, and well-developed mesopores except a bulk Fe content of 2.97 wt% (Figure S8 and Table S6). Strikingly, the $E_{1/2}$ was increased to 0.844 V, which is only 9 mV deviation from the Pt/C catalyst and among the best nonprecious metal catalysts for ORR (Table S5).

To quantify the selectivity of the four-electron reduction of oxygen, a rotating ring-disk electrode (RRDE) technique was conducted to monitor the formation of H_2O_2.[18] The H_2O_2 yield for N-MCNs-22-1000T was maintained below 7% in the full potential range and decreased to 0.6% at 0.8 V, resulting in a high electron transfer number (n) of 3.86–3.99 (Figure 4g), which emphasizes a four-electron ORR mechanism. Furthermore, the Fe-doping endows MCNs with higher n in range of 3.91–4.0. The stability of N-MCNs-22-1000T and N-MCNs-22-Fe-900 was then evaluated by introducing a high

concentration of methanol into the electrolyte.[10] Neither an obvious variation of $E_{1/2}$ nor a crossover effect was observed during this test (Figures 4h and S11), suggesting their promise as cathode catalysts employed in direct methanol alkaline fuel cells. Subsequently, the chronoamperometric (CA) responses of catalysts were examined (Figure 4i).[18,19] N-MCNs-22-1000T and N-MCNs-22-Fe-900 maintained approximately 95% and 97.8% current after 20000 s of continuous operation, whereas Pt/C exhibited a faster and continuous current loss with only 74% current retention, indicating that N-MCNs-22-1000T and N-MCNs-22-Fe-900 have much higher cycling stability compared to commercial Pt/C.

To demonstrate the potential application of our catalyst, we constructed a beaker-type Zn-air battery with N-MCNs-22-Fe-900 catalyst loaded onto the gas diffusion layer as the air cathode and Zn foil as the anode. The state-of-the-art Pt/C catalyst was also tested under the same condition for comparison. The zinc–air battery assembled from our Fe-doped MCNs generates quite stable voltages of 1.32 and 1.23 V at 1 and 10 $mA cm^{-2}$, which are only slightly lower than Pt/C (Figure S12a–b), and comparable to other high-performance nonprecious metal catalysts.[20] Notably, at a high current density of 100 $mA cm^{-2}$, the voltage gap between Fe-doped MCNs and Pt/C cathodes gradually disappeared (Figure S12c), indicating the high ORR activity of Fe-doped MCNs for practical application.

Other than MCNs, our strategy can also be applied to the fabrication of mesoporous PANI nanospheres (MPNs) without pyrolysis (Scheme S2). The as-formed MPNs presented uniform sphere sizes (125–284 nm), tailored mesopores (7–42 nm), and high surface area (42–66 $m^2 g^{-1}$; Figure S13 and Tables S7, S8). When used as active materials for supercapacitors, MPNs-42 delivered specific capacitances of 694, 554, 469, 391, and 336 $F g^{-1}$ at current densities of 0.5, 1, 2, 5, and 10 $A g^{-1}$ (Figure S16c), respectively, which are over 1.5 times the performance of nonporous PANI at the same current density. MPNs-42 also displayed higher capacitance retention of 90% compared to nonporous PANI (83%) after 500 cycles (Figure S16d).

In summary, we developed a method for the controlled synthesis of N-MCNs through self-assembly of colloidal silica. The mesopore size, surface area, pore volume, spherical size, and chemical composition of N-MCNs can be conveniently modulated by varying the reaction parameters, such as templates, feed ratio, precursors, and pyrolysis temperature. The commercial colloidal silica, a versatile and affordable template, used in our strategy guarantees a cost-effective synthesis procedure suitable for industrial production. N-MCNs with a mesopore size of 22 nm, compared to those of 7 and 42 nm, exhibit the best ORR performance in alkaline medium, making it a promising ORR catalyst. By selecting proper precursors and colloidal templates, which will effectively interact with each other, our strategy can be further adapted to prepare various polymers, metal oxides, or metal-doped carbons with controlled morphologies and mesopore sizes.

[1] a) T.-W. Kim, P.-W. Chung, I. I. Slowing, M. Tsunoda, E. S. Yeung, V. S. Y. Lin, *Nano Lett.* **2008**, *8*, 3724–3727; b) Y. Fang, D. Gu, Y. Zou, Z. Wu, F. Li, R. Che, Y. Deng, B. Tu, D. Zhao, *Angew. Chem. Int. Ed.* **2010**, *49*, 7987–7991; *Angew. Chem.* **2010**, *122*, 8159–8163; c) S. Wang, W.-C. Li, G.-P. Hao, Y. Hao, Q. Sun, X.-Q. Zhang, A.-H. Lu, *J. Am. Chem. Soc.* **2011**, *133*, 15304–15307; d) Z.-A. Qiao, B. Guo, A. J. Binder, J. Chen, G. M. Veith, S. Dai, *Nano Lett.* **2012**, *12*, 207–212; e) J. Schuster, G. He, B. Mandlmeier, T. Yim, K. T. Lee, T. Bein, L. F. Nazar, *Angew. Chem. Int. Ed.* **2012**, *51*, 3591–3595; *Angew. Chem.* **2012**, *124*, 3651–3655; f) K. Ai, Y. Liu, C. Ruan, L. Lu, G. Lu, *Adv. Mater.* **2013**, *25*, 998–1003; g) C. Han, S. Wang, J. Wang, M. Li, J. Deng, H. Li, Y. Wang, *Nano Res.* **2014**, *7*, 1809–1819.

[2] J. E. Hampsey, Q. Hu, Z. Wu, L. Rice, J. Pang, Y. Lu, *Carbon* **2005**, *43*, 2977–2982.

[3] a) J. E. Hampsey, Q. Hu, L. Rice, J. Pang, Z. Wu, Y. Lu, *Chem. Commun.* **2005**, 3606–3608; b) Y. Yan, F. Zhang, Y. Meng, B. Tu, D. Zhao, *Chem. Commun.* **2007**, 2867–2869.

[4] J. Tang, J. Liu, C. Li, Y. Li, M. O. Tade, S. Dai, Y. Yamauchi, *Angew. Chem. Int. Ed.* **2015**, *54*, 588–593; *Angew. Chem.* **2015**, *127*, 598–603.

[5] a) C. S. Kong, D.-Y. Kim, H.-K. Lee, Y.-G. Shul, T.-H. Lee, *J. Power Sources* **2002**, *108*, 185–191; b) M. Hartmann, *Angew. Chem. Int. Ed.* **2004**, *43*, 5880–5882; *Angew. Chem.* **2004**, *116*, 6004–6006.

[6] a) S. H. Joo, S. J. Choi, I. Oh, J. Kwak, Z. Liu, O. Terasaki, R. Ryoo, *Nature* **2001**, *412*, 169–172; b) H. Du, L. Gan, B. Li, P. Wu, Y. Qiu, F. Kang, R. Fu, Y. Zeng, *J. Phys. Chem. C* **2007**, *111*, 2040–2043; c) J. Tang, J. Liu, N. L. Torad, T. Kimura, Y. Yamauchi, *Nano Today* **2014**, *9*, 305–323.

[7] a) J. Maruyama, K.-i. Sumino, M. Kawaguchi, I. Abe, *Carbon* **2004**, *42*, 3115–3121; b) W. Wei, H. Liang, K. Parvez, X. Zhuang, X. Feng, K. Mullen, *Angew. Chem. Int. Ed.* **2014**, *53*, 1570–1574; *Angew. Chem.* **2014**, *126*, 1596–1600.

[8] J. Liu, S. Z. Qiao, H. Liu, J. Chen, A. Orpe, D. Zhao, G. Q. Lu, *Angew. Chem. Int. Ed.* **2011**, *50*, 5947–5951; *Angew. Chem.* **2011**, *123*, 6069–6073.

[9] a) H. W. Liang, X. Zhuang, S. Bruller, X. Feng, K. Mullen, *Nat. Commun.* **2014**, *5*, 4973; b) H.-W. Liang, W. Wei, Z.-S. Wu, X. Feng, K. Müllen, *J. Am. Chem. Soc.* **2013**, *135*, 16002–16005; c) Y. Meng, D. Voiry, A. Goswami, X. Zou, X. Huang, M. Chhowalla, Z. Liu, T. Asefa, *J. Am. Chem. Soc.* **2014**, *136*, 13554–13557.

[10] W. Zhang, Z.-Y. Wu, H.-L. Jiang, S.-H. Yu, *J. Am. Chem. Soc.* **2014**, *136*, 14385–14388.

[11] R. Liu, Y. Shi, Y. Wan, Y. Meng, F. Zhang, D. Gu, Z. Chen, B. Tu, D. Zhao, *J. Am. Chem. Soc.* **2006**, *128*, 11652–11662.

[12] a) D. Wu, Z. Li, M. Zhong, T. Kowalewski, K. Matyjaszewski, *Angew. Chem. Int. Ed.* **2014**, *53*, 3957–3960; *Angew. Chem.* **2014**, *126*, 4038–4041; b) Y. Fang, Y. Lv, F. Gong, Z. Wu, X. Li, H. Zhu, L. Zhou, C. Yao, F. Zhang, G. Zheng, D. Zhao, *J. Am. Chem. Soc.* **2015**, *137*, 2808–2811.

[13] Q. Huo, D. I. Margolese, U. Ciesla, D. G. Demuth, P. Feng, T. E. Gier, P. Sieger, A. Firouzi, B. F. Chmelka, *Chem. Mater.* **1994**, *6*, 1176–1191.

[14] R. Silva, D. Voiry, M. Chhowalla, T. Asefa, *J. Am. Chem. Soc.* **2013**, *135*, 7823–7826.

[15] a) R. A. Sidik, A. B. Anderson, N. P. Subramanian, S. P. Kumaraguru, B. N. Popov, *J. Phys. Chem. B* **2006**, *110*, 1787–1793; b) T. Ikeda, M. Boero, S-F. Huang, K. Terakura, M. Oshima, J.-i. Ozaki, *J. Phys. Chem. C* **2008**, *112*, 14706–14709.

[16] W. He, C. Jiang, J. Wang, L. Lu, *Angew. Chem. Int. Ed.* **2014**, *53*, 9503–9507; *Angew. Chem.* **2014**, *126*, 9657–9661.

[17] F. Jaouen, E. Proietti, M. Lefevre, R. Chenitz, J.-P. Dodelet, G. Wu, H. T. Chung, C. M. Johnston, P. Zelenay, *Energy Environ. Sci.* **2011**, *4*, 114–130.

[18] H. X. Zhong, J. Wang, Y. W. Zhang, W. L. Xu, W. Xing, D. Xu, Y. F. Zhang, X. B. Zhang, *Angew. Chem. Int. Ed.* **2014**, *53*, 14235–14239; *Angew. Chem.* **2014**, *126*, 14459–14463.

[19] a) Y. Zhang, X. Zhuang, Y. Su, F. Zhang, X. Feng, *J. Mater. Chem. A* **2014**, *2*, 7742–7746; b) Z. Li, G. Li, L. Jiang, J. Li, G. Sun, C. Xia, F. Li, *Angew. Chem. Int. Ed.* **2015**, *54*, 1494–1498; *Angew. Chem.* **2015**, *127*, 1514–1518.

[20] a) R. Cao, R. Thapa, H. Kim, X. Xu, M. Gyu Kim, Q. Li, N. Park, M. Liu, J. Cho, *Nat. Commun.* **2013**, *4*, 2076; b) Z. Y. Wu, X. X. Xu, B. C. Hu, H. W. Liang, Y. Lin, L. F. Chen, S. H. Yu, *Angew. Chem. Int. Ed.* **2015**, *54*, 8179–8183; *Angew. Chem.* **2015**, *127*, 8297–8301.